

Hydrogen-Atom Binding Energy of Structurally Well-defined Cerium Oxide Nodes at the Metal–Organic Framework-Liquid Interfaces

Zachary J. Ingram,[†] Chance W. Lander,[†] Madeleine C. Oliver,[‡] Nazmiye Gökçe Altınçekiç,[†]

Liangliang Huang,[‡] Yihan Shao,[†] and Hyunho Noh^{†*}

[†]Department of Chemistry and Biochemistry, and [‡]School of Chemical, Biological, and Materials Engineering, University of Oklahoma, Norman, OK 73019, USA

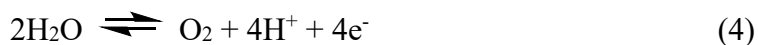
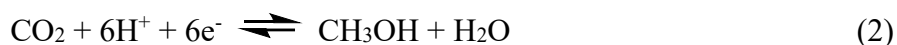
KEYWORDS Proton-Coupled Electron Transfer, Metal–Organic Frameworks, Electrochemistry, Renewable Energy, Cerium Oxide

ABSTRACT Redox-active metal oxides are prevalent in the fields of thermal, photo-, and electrocatalysis. Thermodynamics of proton-coupled electron transfer (PCET) reactions at their surfaces are critical as they *scale* with their activity as a catalyst. The structural heterogeneity and ambiguity of surface sites have largely precluded structural understanding of the exact redox-active sites, challenging chemists to design the catalyst structure down to the atomic level. Here, we report electrochemically determined stoichiometry and thermodynamics of PCET reactions of the cerium-based metal–organic framework (MOF), Ce-MOF-808. Cyclic voltammograms (CVs) of the MOF-deposited electrodes in aqueous buffers at various pHs revealed a Faradaic couple that can be ascribed to Ce^{4+/3+} redox. Plotting the half-wave potential

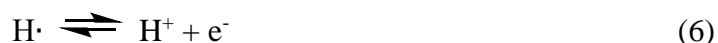
($E_{1/2}$) against the electrolyte pH resulted in a Pourbaix diagram with a slope of 65 ± 9 mV/pH, suggesting a $1\text{H}^+/1\text{e}^-$ stoichiometry. Using the thermochemical analogy between $1\text{H}^+/1\text{e}^-$ and one H-atom ($\text{H}\cdot$), the H-atom binding energy on the hexanuclear Ce_6 node, the $\text{Ce}^{3+}\text{O}-\text{H}$ bond dissociation free energy (BDFE), was calculated to be 77 ± 2 kcal mol $^{-1}$. *In-silico* calculations quantitatively corroborated our BDFE measurements. Furthermore, multiple proton topologies were computationally elucidated to exhibit similar BDFEs to the experimental values, agreeing with the wide Faradaic features of all CVs, implicating that the system has a substantial BDFE distribution. To the best of our understanding, this is the first thermochemical measurement of H-atom binding on MOFs. Implications of the presented thermochemical measurements on catalysis using metal oxides and MOFs are discussed.

INTRODUCTION

Heterogeneous electrocatalysts are essential to shifting the energy and chemical sectors away from fossil fuels to more renewable and sustainable sources. Reducing equivalences harnessed through solar/wind-powered electricity can be funneled to the catalyst that further converts water, CO_2 , and/or N_2 to value-added chemical feedstocks; these include but are not limited to, H_2 , methanol, and ammonia (eqs. 1-3). The generated ‘holes’ during these reactions can be consumed by coupling these reductions with an oxidative reaction, most commonly H_2O oxidation to O_2 (eq. 4).^{1,2}



Many candidate electrocatalysts of the above reactions are redox-active metal oxides that undergo proton-coupled electron transfer (PCET) reactions.^{1,3-6} This is a direct consequence of nearly all energy-relevant reactions involving protons (H⁺'s) and electrons (e⁻'s), which in many cases are equimolar as shown above. Surfaces of metal oxides in contact with protic medium are often rich in proton donors and acceptors such as surface oxo, hydroxyl, and aqua groups.⁷⁻¹⁰ The electrons are transferred to and from the metal cations, which can be delocalized depending on their electronic properties.¹¹⁻¹³ Taking cerium oxide (CeO₂) as a case study, surface PCET reaction involves a change in Ce^{4+/3+} redox states and a simultaneous surface protonation/deprotonation (eq. 5).¹⁴⁻¹⁷ Because an H-atom is thermochemically equivalent to H⁺ and e⁻, this so-called Volmer reaction is consequently equivalent to a Ce³⁺O–H bond formation (eqs. 6 and 7).^{18,19}



Thermodynamics of H-atom transfer plays a critical role in the field of surface science and heterogeneous catalysis.^{1,20-22} The free energy to homolytically cleave the surface O–H bonds, the O–H bond dissociation free energy (BDFE), is a commonly known thermochemical value associated with metal oxides.^{13-15,18,19,23,24} It is thermochemically equivalent to the more general, H-atom binding energy ($\Delta G^\circ_{\text{H}}$).⁶ These values must be neither too strong nor too weak for optimal catalytic performance. Catalysts with low binding energies are kinetically limited by the low surface population of necessary H-atoms. Excessive binding energies, on the other hand, will saturate the catalyst surface with unreactive H-atoms that impede the overall reaction rate. This so-called Sabatier Principle is further highlighted by the ‘volcano-type’ plot that correlates $\Delta G^\circ_{\text{H}}$

of various catalysts to their catalytic performances. This approach has proven to be a powerful tool to rationalize and even predict the activities of electrocatalysts in energy-relevant reactions that involve PCET reactions.^{1,4,21,25,26}

Despite the widespread use of the Sabatier Principle, the structural heterogeneity and ambiguity of surface catalytic sites pose a challenge to its application.^{6,25} The common approach is to computationally derive H-atom binding energies on various materials and their crystal facets, and further compare those values to the experimentally observed catalytic activity.^{1,21,26} The use of defect-free crystalline surfaces as a computational model, however, can result in discrepancies in stoichiometry, structure, and other chemical properties of the *actually* employed catalyst. This is particularly pronounced in metal oxides and other binary materials where the surface structure is quite complex. Indeed, a few reported H-atom binding energies that were experimentally measured on binary materials have proven to be distinct from and have a wide range of distribution as compared to the computationally derived values.^{14,19,27-29} The apparent enhancement in electrocatalytic activity that involves multiple PCET reactions (*e.g.*, water oxidation) upon surface amorphization of many metal oxides further questions whether the *in-silico* derived $\Delta G^\circ_{\text{H}}$ values are representative of the actual catalytic sites.³⁰⁻³³

Metal–organic frameworks (MOFs) with redox-active inorganic nodes offer a unique opportunity to examine the thermodynamics of H-atom binding with atomic-level structural precision. MOFs with multinuclear metal-oxo nodes with terminally bound –OH/–OH₂ groups are of particular interest as locally, the nodes structurally mimic the surfaces of bulk metal oxides.³⁴⁻³⁶ These metal-oxo clusters are dispersed throughout the porous network that allows efficient diffusion of necessary substrates and products – *i.e.*, all nodes essentially behave as ‘surface sites.’ Crystallinity further ensures the periodicity and uniformity of each redox-active

site, and thus experimental and computational measurements of thermochemical values can be performed on the *identical* structure. Indeed, these systems lend themselves well to structure-activity relationships grounded by atomic-level mechanistic studies for a wide variety of thermal, photochemical, and electrochemical reactions.^{34,36-44}

Herein, we report the electrochemically derived thermochemical measurements of PCET reactions using a representative Ce-based MOF, Ce-MOF-808 (Figure 1).⁴⁵ The nodes of this MOF, $\text{Ce}_6(\mu_3\text{-O})_4(\mu_3\text{-OH})_4(\text{OH})_6(\text{H}_2\text{O})_6$ have up to six Ce cations that can undergo $\text{Ce}^{4+/3+}$ redox reactions.⁴⁶⁻⁴⁸ The $-\text{OH}/-\text{OH}_2$ groups can concurrently transfer the necessary H^+ . The nodes are connected with 1,3,5-benzene tricarboxylate (BTC^{3-}) linkers to yield a large pore with 18 Å aperture, allowing efficient diffusion of electrolytes to the redox-active nodes. The PCET nature of the $\text{Ce}^{4+/3+}$ redox reactions on Ce-MOF-808 and many other Ce-based MOFs have previously been inferred,^{48,49} but its proton-to-electron stoichiometry remains to be validated. Our electrochemical measurements indicated the $1\text{H}^+/1\text{e}^-$ stoichiometry during the PCET reaction and further derived the $\text{Ce}^{3+}\text{O}-\text{H}$ BDFE on these nodes. To the best of our understanding, this is the first report of experimentally derived thermochemical values at MOF-liquid interfaces. BDFE values were further computationally corroborated by assessing various proton topologies of the nodes. Implications of these results are contrasted to the thermochemical and catalytic measurements of other MOF-based catalysts and metal oxides.

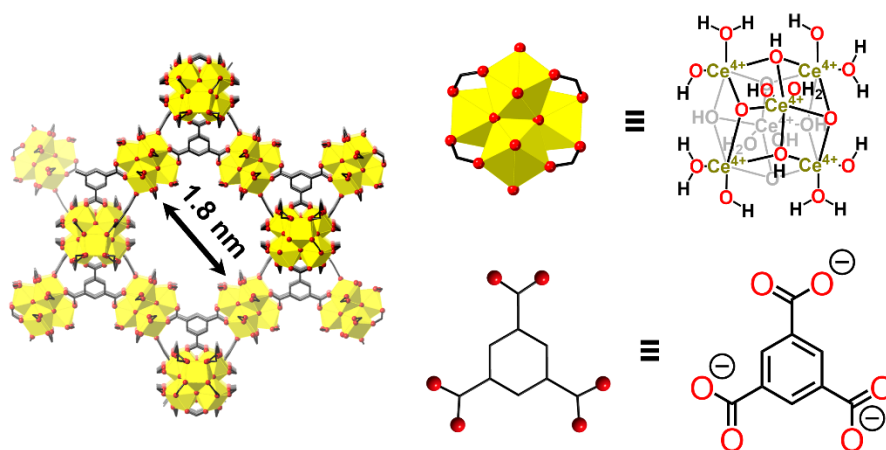


Figure 1. Structures of Ce-MOF-808 and its nodes/linkers.

RESULTS

General Considerations of Ce-MOF-808-based Electrodes

Ce-MOF-808 was synthesized according to the reported procedure.⁴⁹ The porosity, crystallinity, and particle morphologies were confirmed through N₂ adsorption-desorption isotherms, powder X-ray diffraction (PXRD) pattern, and scanning electron microscopy (SEM) images, respectively; see Figures S1-S3 in the Supporting Information (SI) for details.

Ce-MOF-808-based electrodes were prepared through a simple drop-casting method on fluorine-doped tin oxide (FTO) electrodes with a polyimide tape to control the electroactive area as reported previously.⁴⁹ This electrode here onwards is referred to as Ce-MOF-808|FTO. The amount of Ce-MOF-808 loaded per sample was determined by digesting in ~1 M NaOD in D₂O and measuring the ¹H NMR spectra (Figure S4). Polymeric binders or carbon nanotubes used in the reported procedure⁴⁹ were avoided as they are known to exhibit PCET reactivity and/or alter physical and chemical properties such as hydrophilicity or proton activity near the electrochemical double layer that obscures the thermochemical measurements of Ce^{4+/3+} redox reactions.^{50,51} All electrochemical measurements of Ce-MOF-808 were performed in pH-adjusted aqueous electrolytes with 100 mM NaCl and 100 mM of buffers, such as 3-morpholinopropane-

1-sulfonic acid (MOPS), Tris(hydroxymethyl)aminomethane (Tris), and boric acid. Unless otherwise noted, all cyclic voltammograms (CVs) were measured with a scan rate (v) of 25 mV/s. Further details of the electrochemical setup can be found in the SI.

CVs of Ce-MOF-808|FTO in Buffered Aqueous Electrolytes

CVs of Ce-MOF-808|FTO measured within the pH range of 7–10 all revealed one reversible Faradaic couple (Figure 2A). Previously reports of Ce-MOF-808-based electrodes and CeO₂ have presented similar electrochemical responses.^{49,52} Thus, we have concluded the observed Faradaic feature to be Ce^{4+/3+} redox reaction.

The half-wave potential ($E_{1/2}$) derived from the CVs scaled linearly with respect to the electrolyte pH with a slope of 65 ± 9 mV/pH. The close-to-Nernstian slope of 59 mV/pH suggests a $1\text{H}^+/1\text{e}^-$ stoichiometry (Figure 2B).^{15,18,19,53-58} $E_{1/2}$ measured at the same pH with *different buffers* were mostly within ± 50 mV difference, suggesting that the Ce^{4+/3+} redox is independent of the proton source. Combining these results with the previous thermochemical measurements of bulk ceria,^{14,15,59} we ascribe the Ce^{4+/3+} redox reaction to a $1\text{H}^+/1\text{e}^-$ PCET reaction (eq. 8).

The Ce₆ node has six pairs of terminally-bound –OH/–OH₂ groups and four pairs of μ_3 -O/OH groups that can all act as a proton donor and/or acceptor. The presented electrochemical measurements *do not indicate* the exact proton topology of the reduced and oxidized nodes. Thus, nodes in the two states in eq. 8 are written without an explicit proton topology.

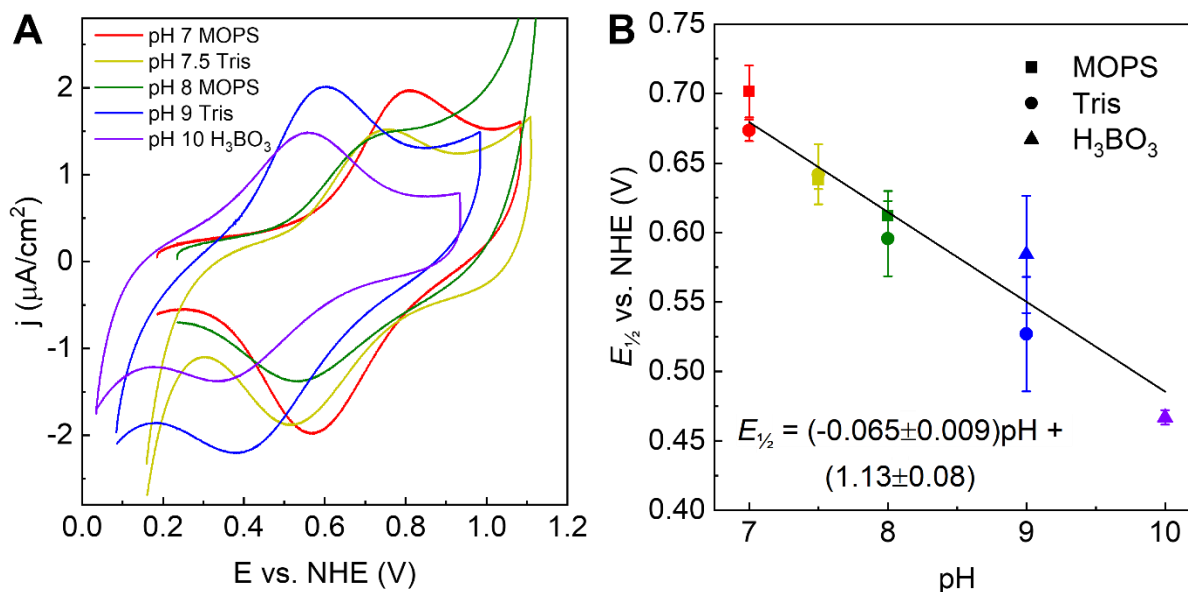
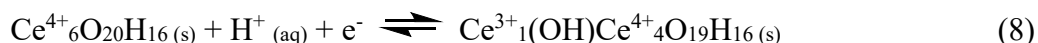


Figure 2. Electrochemical results of Ce-MOF-808|FTO in pH-adjusted aqueous electrolytes. **(A)** CVs of Ce-MOF-808 in five representative electrolytes. Others can be found in the SI. **(B)** A plot of CV-derived $E_{1/2}(\text{Ce}^{4+/3+})$ plotted against the electrolyte pH. The error bars represent 1σ of three separate measurements using a freshly prepared Ce-MOF-808|FTO.



An ideal CV of a heterogenized redox-active species has equal values of the peak anodic and cathodic currents ($j_{p,a}/j_{p,c} = 1$), no peak separations ($\Delta E_p = 0$ mV), and a full-width at half-maximum (FWHM) of 90 mV.⁶⁰ At all pHs and buffers used in this study, the Faradaic features of Ce-MOF-808|FTO deviated, but with varying extent, from these ideal values (Table S1 and Figures S5-S7). $j_{p,a}/j_{p,c}$, and ΔE_p were somewhat pH-dependent. Within the pH range of 7–8, $j_{p,c}$ was roughly twice as large as $j_{p,a}$, while at pH 9 and 10, $j_{p,a}$ was nearly equal to or larger than $j_{p,c}$. All ΔE_p values were at least 200 mV and decreased as a function of pH. The FWHM values were larger than the ideal 90 mV and were independent of the pH. Deviations of CVs from the

idealized values have been reported previously on Ce-MOF-808, bulk ceria, and many other metal oxides.^{15,19,29,49,61-64}

CVs with varying v between 10 to 100 mV/s were collected in a pH 8-adjusted Tris buffer as a representative electrolyte. $E_{1/2}$ remained largely consistent while the ratio, $j_{p,a}/j_{p,c}$, decreased with an increasing v (Table S2 and Figure S8). The slopes of the logarithms of v and the two peak currents are indicative of the electrochemical mechanism. A slope of $1/2$ indicates a diffusion-controlled reaction, while a slope of 1 suggests a reaction controlled by the kinetics of the PCET reaction.⁶⁵ Plots using $j_{p,a}$ and $j_{p,c}$ both showed near unity slope (Figure S9), though the slope of $\log(j_{p,a})$ vs. $\log(v)$ was slightly lower, suggesting that the oxidation of Ce^{3+} to Ce^{4+} is perhaps more sensitive to the diffusion.

Combining all electrochemical measurements, the close-to-Nernstian $E_{1/2}$ dependence with respect to the electrolyte pH suggests that Ce-MOF-808 undergoes a $1\text{H}^+/1\text{e}^-$ redox reaction. Thus, the modified version of the Nernst equation explicitly showing the fractional surface coverages (θ) of the two redox states, $\text{Ce}^{4+/3+}$ (eq. 9), is representative of the experimentally observed results.¹⁹

$$E = E^\circ - 0.0591 \log \left(\frac{\theta_{\text{Ce}^{3+}}}{\theta_{\text{Ce}^{4+}}} \right) - 0.0591 \text{pH} \quad (9)$$

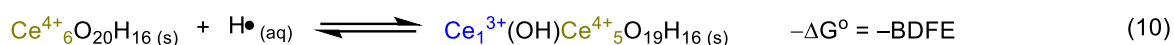
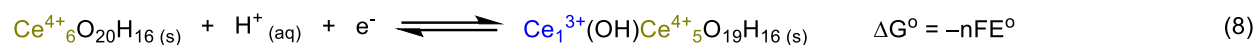
Under all reaction conditions, PXRD patterns of Ce-MOF-808 remained identical before and after an electrochemical treatment (Figure S2). We conclude that the MOF structure remains intact throughout all experiments, and the bulk crystal structure of Ce-MOF-808 is representative of that under electrochemical conditions.

Electrochemically Derived $\text{Ce}^{3+}\text{O}-\text{H}$ BDFE of Ce-MOF-808

The $1\text{H}^+/1\text{e}^-$ stoichiometry of the $\text{Ce}^{4+/3+}$ redox reaction establishes that this PCET reaction is a *net H-atom transfer occurring on the node* (eq. 10 in Scheme 1).^{6,18} The thermodynamic

potential of this redox reaction (E°), together with the free energy to form H-atom from H^+ and e^- (C_G) yields the Bordwell equation (eq. 11) that can be applied to determine $Ce^{3+}O-H$ BDFE.¹⁸

Scheme 1. $Ce^{3+}O-H$ BDFE Derivation of Ce-MOF-808|FTO



$$BDFE(Ce^{3+}O-H) = 23.06E^\circ(Ce^{4+/3+} \text{ vs. NHE at pH} = 0) + C_G \quad (11)$$

Two E° values were derived by extrapolating the linear trend between $E_{1/2}$ and pH (Figure 2B) to pH of 0 using the fitted linear curve or by enforcing a 59 mV/pH slope (see Table S3 in the SI). By using the average of the two E° values and eq. 11, the $Ce^{3+}O-H$ BDFE was derived to be $77 \pm 2 \text{ kcal mol}^{-1}$, which is within the range of measured BDFEs on various cerium oxides.^{14,15,66,67}

Computational Calculations of H-atom Transfer Thermochemistry on Ce Nodes of Ce-MOF-808

Using the experimentally derived $Ce^{3+}O-H$ BDFE as a benchmark, *in-silico* calculations with multiple simulation packages, functionals, basis sets, and other parameters were attempted on a single Ce_6 node terminated with six formate linkers, following the method reported previously.⁴¹ In this section, we describe the results from using the PBE0 functional⁶⁸ as implemented in Q-Chem 6.1, given the closest quantitative agreement with the experimental results; efforts using CP2K^{69,70} are described in the SI. The 6-31G* basis set⁷¹ was used for all first and second-row elements, while the SRSC basis set and effective core potential (ECP)⁷² were used for Ce. The self-consistent field (SCF) energy was converged using the pseudo-fractional occupation number method.⁷³

Each Ce₆ node in its oxidized state has two possible Brønsted base sites: the bridging μ₃-O and the terminal -OH groups. In addition, the formed O-H bonds can have two distinct distances from the organic linkers (which is a formate unit in the simulations), as the Ce₆ nodes are six-connected. In total, four different proton topologies upon an H-atom binding event were considered and their electronic energies were used to estimate the Ce³⁺O-H BDFE values. The resulting structure and their energies are illustrated in Figure 3 and Table 1.

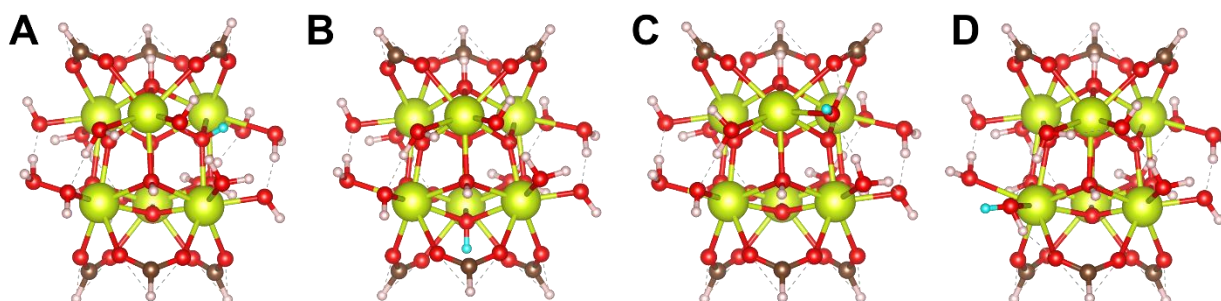


Figure 3. Computationally simulated, geometrically optimized Ce₆ nodes of Ce-MOF-808. The extra protons added upon a PCET reaction (shown in cyan) are added on (A-B) μ₃-O or (C-D) terminal -OH groups. Ce, O, C, and H-atoms (other than the extra proton) are denoted in yellow, red, brown, and white, respectively.

Table 1. Computationally Derived Thermochemical and Structural Parameters of Reduced Ce₆ Nodes with Various Proton Topologies

Parameter	Proton Topology ^a			
	A	B	C	D
Thermochemical Parameter (kcal mol ⁻¹)				
Ce ³⁺ O-H BDFE	81.9	79.8	90.2	84.5
Distance Changes (Å) ^b				
Ce-O(H) ^c	0.2	0.2	0.5	0.5

(H ₂)O–O(H ₂)	–	–	0.2	0.3
(H ₂)O–O(linker)	–	–	–0.2	–0.3

^aThe labels of the proton topology correspond to those in Figure 3. ^bThese are derived by subtracting the bond distance of the oxidized Ce₆ node from that reduced. Therefore, positive and negative values refer to bond elongation or contraction upon reduction, respectively. For the exact bond distances of the two nodes, see the SI. ^cFor proton topologies A and B, the average Ce–O(H) distance between the three neighboring Ce atoms was calculated.

The reduced Ce₆ nodes with an additional proton to yield μ₃–OH (Figures 3A and B) exhibited Ce³⁺O–H BDFE values of 81.9 and 79.8 kcal mol^{–1}, closely agreeing with the experimentally derived value. The BDFE values with the additional, terminal –OH₂ group were slightly larger (90.2 and 84.5 kcal mol^{–1}). Concurrent with H-atom binding, significant geometric rearrangements were observed regardless of its final proton topology. Upon protonation of μ₃–O, the Ce–O bonds between the three neighboring Ce cations elongate by ~0.2 Å (see the SI for details). Similar bond elongation can be observed for the terminal Brønsted base. Formation of two terminally bound, –OH₂ groups further lead to a change in their distances; the newly formed aqua group undergoes an H-bonding with the O-atom from the carboxylate, effectively decreasing the (H₂)O–O(linker) distance by ~0.1 Å.

In sum, using the geometrically optimized structures of reduced Ce₆ node, Ce³⁺O–H BDFE values were largely consistent with the experimentally derived values. Implications of these calculations are elaborated in the Discussion section.

DISCUSSION

PCET Reactions at the Ce₆ Nodes

The Faradaic features observed in the CVs of Ce-MOF-808 are ascribed to the PCET reactions on the hexanuclear Ce₆ nodes. The CV-derived *E*_{1/2} values shift with the proton activity of the aqueous electrolytes and are predictable by the Nernst equation (eq. 9). Slight deviation of the slope from 59 mV/pH is attributed to the small kinetic/diffusive complications, indicated by the

scan rate dependence and other measurements. These deviations are expected for electrochemical measurements with porous materials and have been observed previously for many other MOF-based systems.^{49,74-76} Nevertheless, the Nernstian slope still constitutes Ce-MOF-808|FTO as a ‘well-behaved’ system to derive H-atom transfer thermodynamics electrochemically.

The thermodynamics of this PCET reaction is *independent* of the proton donors and acceptors within the electrolyte. Three buffers with distinct protic groups were employed. MOPS buffer with a weakly coordinating sulfonate group likely leaves the bridging and terminal –OH/–OH₂ groups on the nodes intact, while borate anions can bind as it does on the surfaces of nickel and other metal oxides.^{61,62} The large pore aperture of 1.8 nm of Ce-MOF-808 suggests that all buffer species can diffuse into the MOF lattice. However, intracrystalline diffusion within the porous network, particularly of those as large as MOPS molecules, is known to be slow;^{77,78} as the relevant redox reactions occur very close to the FTO electrode, the slow diffusion from the bulk electrolyte could obscure the thermodynamics. Yet, the measured $E_{1/2}$ scaled *in a single linear function* with respect to pH, suggesting that the buffer identity does not lead to changes in the PCET reaction thermodynamics.

This buffer independence is not a universal characteristic of binary materials. CVs of nickel and cobalt layered double hydroxides (LDHs) have distinct $E_{1/2}$ values depending on the anions within the electrolyte (*e.g.*, phosphate, borate, etc.).^{61,79} This has also been observed recently on layered hydrogen titanate (H₂Ti₃O₇).⁸⁰ When bunsenite nickel oxide is used as the electrode instead, its Faradaic features are independent of the buffers, supporting electrolytes, and even solvents.^{19,23} In the latter system, the observed medium independence was ascribed, at least in part, to a small fraction of *surface* Ni sites solely being electrochemically active; this contrasts with LDHs that have up to near-unity addressability owing to their layered structure that allows diffusion of

electrolytes throughout its lattice.^{81,82} The low electrochemical addressability of Ce-MOF-808|FTO is ascribed to its low electrical conductivity;⁸³ in other words, the observed electrochemical response must *solely* arise from the Ce₆ nodes near the underlying FTO surface. The ‘effective concentration’ of Ce₆ nodes within the lattice is at least several hundred millimolar, and all Ce cations are in contact with the liquid medium.⁴² Thus, it is still tempting to correlate the Ce cations within the node to be *more similar than different* to metal cations within LDHs. The observed buffer independence does *not* rule out buffer-node interactions (cf. ¹⁹ for details).

In sum, the redox reaction of the Ce₆ node can be described as a *simple* PCET reaction that solely involves protons like that shown in eq. 8. The close-to-Nernstian dependence of $E_{1/2}$ vs. pH established the stoichiometry of the H⁺ and e⁻ to be 1:1. The thermodynamic potential can hence be derived from electrochemical measurements.

H-atom Transfer Thermochemistry of Ce-MOF-808

With the buffer independence and H⁺/e⁻ stoichiometry established, we experimentally derived the average Ce³⁺O–H BDFE of Ce-MOF-808 to be 77 ± 2 kcal mol⁻¹. The buffer independence further *simplified* our computational simulations. The source of protons is unnecessary to be considered in determining the *thermodynamics* of the PCET reaction. Further, by considering the observed reaction as a net H-atom transfer reaction, the addition and removal of H-atom to and from the node largely avoided unstable intermediates that obscure the simulation.

The structural knowledge of Ce₆ nodes of Ce-MOF-808 enabled simulations with atomic-level precision. The close agreement in thermochemistry between experimental and computational results was surprising given the reported challenges of a system with multiple lanthanides, including Ce cations. The differences between the experimental and computational values can be

at least 1 eV (or 23 kcal mol⁻¹).^{84,85} Indeed, our attempts at using CP2K resulted in a large discrepancy in the BDFE values. The use of experimental value as a benchmark enabled the validation of various computational models, with proton topologies simulated by PBE0 functional in Q-Chem 6.1 being our preferred model. The proton topology with the closest match in BDFE value to the experimentally derived one was that with an extra proton being bound to μ_3 -O, with the formed O-H bond pointing towards the linkers (Figure 3B).

Ce³⁺O-H BDFE of Ce-MOF-808 lies within the range of reported values of other Ce-based materials, though the range is relatively large. Extrapolation of the Pourbaix diagram of CeO₂ in the *Atlas of Electrochemical Equilibrium in Aqueous Solutions*, for example, determines the Ce³⁺O-H BDFE to be ~88 kcal mol⁻¹.⁶⁶ BDFEs of molecular complexes with “CeO-H” moieties, as well as colloidal CeO₂ nanoparticles range between 61 to 74 kcal mol⁻¹.^{14,67} The BDFE measurement of heterogenized nanoceria on FTO is particularly noteworthy as the Ce³⁺O-H BDFE was measured to be similar to that of Ce-MOF-808 (79 ± 2 kcal mol⁻¹).¹⁵ The CVs of Ce-MOF-808 and nanoceria on FTO were *qualitatively* similar with large ΔE_p , the $j_{p,a}/j_{p,c}$ ratio deviating from unity, and wide FWHM; implications of these features in the H-atom transfer thermochemistry are discussed in the next section.

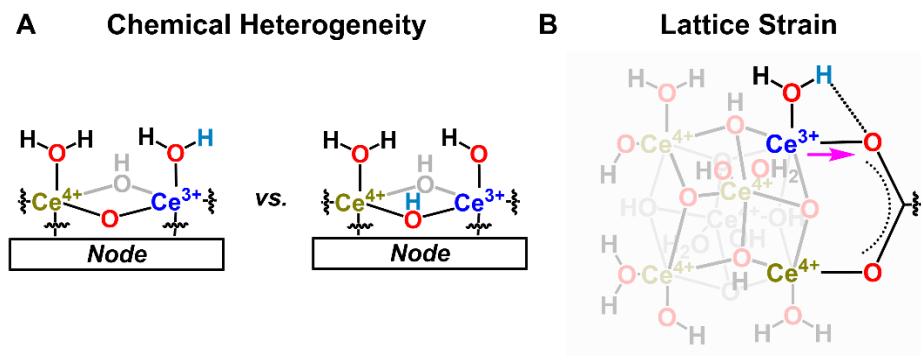
Non-Ideality in H-atom Binding

The wide Faradaic features with FWHM between 200–300 mV and large ΔE_p deviate from the ideal values expected for CVs of heterogenized redox-active species (FWHM = 90 mV, ΔE_p = 0 mV).⁶⁰ While these deviations can partly be ascribed to diffusive/kinetic complications, CVs even with the slowest scan rate of 10 mV/s did not exhibit idealized parameters. Thus, these deviations must arise due to the *non-ideal thermodynamics*.

The origin of the broad Faradaic features has previously been ascribed to lateral interactions between adsorbates and/or chemical heterogeneity.^{19,86} In the former case, the physical and chemical environment of each adsorption site is *intrinsically* identical; however, adsorbates can induce repulsive interactions. Thus, the BDFE of an O–H bond near another is effectively weakened. In the other case, the intrinsic chemical heterogeneity is the origin of the breadth of BDFE distribution. The FWHM values of roughly 200 mV observed in all electrochemical measurements of Ce-MOF-808|FTO corresponds to 6–7 kcal mol⁻¹ width in Ce³⁺O–H BDFE.^{6,19,87}

The four proton topologies computationally assessed for their BDFEs were energetically similar to each other. Their BDFE values matched well to the experimentally observed Ce³⁺O–H BDFE, with the largest deviation being 13 kcal mol⁻¹ (or 0.6 eV); as noted above, the difference in experimentally and computationally derived thermochemical values for the lanthanide-containing systems are often quite large (>1 eV).^{84,85} These relatively small differences between various proton topologies suggest that under the electrochemically biased potential, most if not all of the assessed proton topologies are energetically accessible. Significant rearrangements of atoms neighboring the protonation sites were observed upon reduction, suggesting that the lattice strain induced in the MOF network can further increase the BDFE distribution. Furthermore, Ce³⁺ cations are at least 50% larger in volume than Ce⁴⁺ and have different affinity towards carboxylate groups.^{14,88,89} Perhaps this structural deformation explains the lower stability of Ce-based MOFs, particularly upon a redox reaction, as compared to Zr- and Hf-analogs; it is noteworthy that Zr⁴⁺ and Hf⁴⁺ are largely redox-innocent.⁹⁰ These effects combined most likely in a complex manner, should be the origin of the non-ideality in H-atom binding within Ce-MOF-808 (see Scheme 2).

Scheme 2. Schematic illustration of the possible origins of the breadth in the $\text{Ce}^{3+}\text{O-H}$ BDFE



The observed BDFE distribution of Ce-MOF-808 contradicts the common *implicit* assumption in the field of MOF-based (electro)catalysis. The crystallinity and periodicity of MOFs have been ascribed to yield *single-site* catalysts with identical structure, and therefore, identical thermodynamics and kinetics.^{36,44,91} The experimentally and computationally observed *non-ideality* is strong evidence that *identical catalytic sites can still exhibit a wide range of catalytically relevant thermochemical values, which should impact their overall activity and selectivity, as discussed below.*

Significance of $\text{Ce}^{3+}\text{O-H}$ BDFE Measurement at MOF-Liquid Interfaces

To the best of our understanding, this is the first report of a *quantitative thermochemical measurement of H-atom transfer* at MOF-liquid interfaces. Chemical titrations to bracket the BDFE ranges have been reported for a Ti-based MOF, Ti-MIL-125, but these studies *did not* determine the exact BDFE values.⁹² Other thermochemical values of Ce-based MOFs that focus on the free energy of electrons (*e.g.*, conduction/valence band (CB/VB) energies and the associated band gaps) are available in the literature.^{47,48} The use of band energies of binary materials to describe *PCET reactions*, particularly when the material is in contact with the protic medium, has recently been questioned as it does not consider the thermodynamics of protons.⁶

The proton topologies and the covalent bonds formed or broken during the *inner-sphere PCET reactions* like the observed $\text{Ce}^{3+}\text{O}-\text{H}$ bond cannot be described solely by the energetics of electrons. Band gap energies are often referenced to vacuum and to normal hydrogen electrode (NHE), which implicitly assumes the surface proton topology to be identical in contact under vacuum vs. 1 M acid. As nearly all MOFs decompose in 1 M acid, this seems to neglect the physical properties.⁹³ Proton topologies of isostructural Zr- and Hf-based MOF-808 change as a function of proton activity,⁹⁴ and hence this further assumes that the Ce_6 node proton topologies *do not* affect the PCET thermodynamics, which is unlikely.

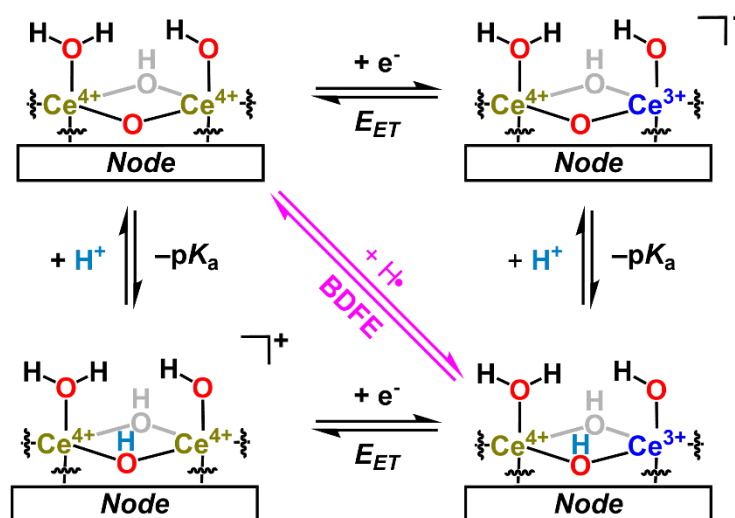
Thermochemical measurements of proton transfers are scarce for Ce-based MOFs. Nevertheless, Ho *et al.* reported lower activation energy (E_a) of H^+ transfer within Ce-MOF-808 as to Zr-MOF-808. Computational calculations have further elucidated up to 20 $\text{p}K_a$ unit differences (in H_2O) between the Brønsted acids on Ce_6 or Zr_6 nodes.⁹⁵ Qualitatively, this $\text{p}K_a$ difference agrees with the observed H^+ conductivity differences. *Quantitatively*, however, a 20 $\text{p}K_a$ unit difference makes the $\text{p}K_a$ of terminal $\text{CeO}-\text{H}$ *ca.* -16 ($\text{p}K_a$ of terminal $\text{ZrO}-\text{H}$ has been experimentally measured to be ~ 4).⁹⁴ This is unlikely given that this $\text{p}K_a$ is lower than strong acids like triflic acid.⁹⁶

H^+ or e^- transfer reactions both yield a charged Ce_6 node. Our initial experimental attempts to chemically reduce Ce-MOF-808 with reductants that *solely* donate electrons led to MOF decomposition. Experimental $\text{p}K_a$ of Ce-MOFs is lacking in the literature given their relatively low hydrochemical stability.⁹⁰ These and many other factors are perhaps the reasons for the lack of reliable thermodynamic parameters that describe the electron/proton transfer reactions, including those shown in the square scheme below (Scheme 3). The advantages of using BDFEs as a thermochemical value to describe PCET reactions have been illustrated in the metal oxide

literature as BDFEs are independent of the proton activity of the liquid medium in contact.^{18,19}

We argue that this advantage is even more pronounced for Ce- and other redox-active MOFs as this treatment avoids high-energy intermediates that can lead to their degradation.

Scheme 3. PCET Square Scheme of Ce₆ Nodes with μ₃-O as the Proton Acceptor



Implications of the Determined Ce³⁺O–H BDFE on Reactions Catalyzed by Ce-MOFs and Cerium Oxides

Ce-MOF-808 has previously been reported to be catalytically active towards the oxidation of benzyl alcohol to benzaldehyde, which involves C–H and O–H bond cleavages, *i.e.*, two H-atom transfer reactions.⁴⁶ Comparison of the substrate vs. catalyst BDFE values is indicative of the reaction thermodynamics. This comparison seemingly is valid even for substrates that undergo multiple H-atom transfer reactions, with quite distinct BDFEs.^{23,97,98} Based on their thermodynamic potentials and by using the Bordwell equation (eq. 11), the average of the C–H and O–H BDFEs of benzyl alcohol is 56 kcal mol⁻¹;⁹⁹ thus using our Ce³⁺O–H BDFE measurements, we can conclude that Ce-MOF-808-catalyzed benzyl alcohol oxidation is thermodynamically downhill by >20 kcal mol⁻¹, agreeing with its high activity. More recently, Chiang *et al.* reported that Ce-MOF-808 can oxidize and reduce dopamine/dopaquinone redox

couple quasi-reversibly.¹⁰⁰ The average O–H bond dissociation enthalpy (BDE) of dopamine has been measured to be *ca.* 78 kcal mol⁻¹.¹⁰¹ For molecules like dopamine and dopaquinone with similar size and polarity, the entropic change during an H-atom transfer is minimal, and thus BDE is nearly identical to BDFE.¹⁸ Indeed, this agrees with the observed reversibility as the BDFEs of Ce-MOF-808 and dopamine are nearly equal, making the overall reaction nearly thermoneutral.

CONCLUSIONS AND FUTURE OUTLOOK

Thermochemistry of H-atom transfer reactions was experimentally and computationally determined on structurally well-defined, Ce₆ node of a MOF, Ce-MOF-808. Electrochemically determined Ce³⁺O–H BDFE of ~77 kcal mol⁻¹ largely agreed with the previously reported BDFE values of other ceria-based materials.^{14,15,66,67} BDFE values were structurally corroborated using computational simulations. We further argue that BDFE should be the preferred thermochemical parameter to describe the energetics of PCET reaction within MOFs that involve equimolar amounts of protons and electrons. The net charge-neutrality avoids unstable intermediates, which for extended lattice structures like MOFs, can lead to an immediate decomposition. Computational simulations of net neutral nodes were more feasible. Integration of experimental and computational efforts with atomic-level structural precision highlights the key advantage of employing MOFs to derive structure-thermochemistry relationships relevant to heterogeneous catalysis and many other fields.

Detailed thermochemical and computational analysis have further eluded *ca.* 6 kcal mol⁻¹ wide distribution of Ce³⁺O–H BDFE that depends on the proton topology of the Ce₆ node. This contrasts with the *implicit assumption* within the MOF field that *structurally identical MOF-embedded sites must have identical thermodynamics*.^{36,44,91} Our computational efforts have

eluded that this distribution is *inherently* related to (1) the presence of up to six Ce cations that can be redox-active and (2) the rich amount of proton donors/acceptors distinct in their geometry. Many Ce-based MOFs distinct in their proton topologies, node nuclearity, oxidation state at its resting state, and many others have been discovered,⁴⁸ and their effects on thermochemistry are our current research focus. The presented work serves as a pivotal example to demonstrate the use of Ce-MOF-808 as a case study for the atomically precise structure-thermochemistry relationship of H-atom transfer reactions.

ASSOCIATED CONTENT

The supporting information is available free of charge.

Physical characterization including N₂ adsorption-desorption isotherm, SEM images, PXRD patterns, detailed analysis of CVs, and details on computational characterization. (PDF)

AUTHOR INFORMATION

Corresponding Author

*Hyunho Noh: Department of Chemistry and Biochemistry, the University of Oklahoma, Norman OK USA 73019; ORCID: 0000-0003-3136-1004

Author Contributions

The manuscript was written through the contributions of all authors. All authors have given approval to the final version of the manuscript.

Z.J.I. and H.N. conducted all physical characterization and electrochemical measurements. C.W.L. and M.C.O. conducted *in-silico* calculations using Q-Chem 6.1 or CP2K under the

supervision of Y.S. and L.H., respectively. N.G.A. repeated the *in-silico* calculations for reproducibility confirmation. The manuscript was written by Z.J.I., C.W.L., M.C.O., and H.N.

Notes

The authors declare no competing financial interest.

ACKNOWLEDGMENT

H.N. is supported by the University of Oklahoma startup funds. Y.S. is supported by the National Science Foundation via grant No. CHE-2102071. L. H. acknowledges the financial support from DTRA through the grant HDTRA1447180. PXRD and microscopy data collections were performed at the Samuel Roberts Noble Microscopy Laboratory, an OU core facility supported by the Vice President for Research and Partnerships. The computing for this project by C.W.L. and Y.S. was performed at the High Performance Computing Center at Oklahoma State University supported in part through the National Science Foundation grant OAC-1531128. M.C.O. and L.H. thank the OU Supercomputing Center for Education & Research (OSCER) at the University of Oklahoma for computational resources and dedicated support. Z.J.I. and H.N. acknowledge Dr. Preston R. Larson for his help during the SEM image processing and the PXRD measurements, and Farzana Akter Runa for several experiments conducted during the initial stage.

REFERENCES

1. Seh, Z. W.; Kibsgaard, J.; Dickens, C. F.; Chorkendorff, I.; Nørskov, J. K.; Jaramillo, T. F., Combining theory and experiment in electrocatalysis: Insights into materials design. *Science* **2017**, 355 (6321), eaad4998.
2. Zhao, S.; Yang, Y.; Tang, Z., Insight into Structural Evolution, Active Sites, and Stability of Heterogeneous Electrocatalysts. *Angew. Chem. Int. Ed.* **2022**, 61 (11), e202110186.

3. Zhu, Y.; Lin, Q.; Zhong, Y.; Tahini, H. A.; Shao, Z.; Wang, H., Metal oxide-based materials as an emerging family of hydrogen evolution electrocatalysts. *Energy Environ. Sci.* **2020**, *13* (10), 3361-3392.
4. Tao, H. B.; Fang, L.; Chen, J.; Yang, H. B.; Gao, J.; Miao, J.; Chen, S.; Liu, B., Identification of Surface Reactivity Descriptor for Transition Metal Oxides in Oxygen Evolution Reaction. *J. Am. Chem. Soc.* **2016**, *138* (31), 9978-9985.
5. Nocera, D. G., Proton-Coupled Electron Transfer: The Engine of Energy Conversion and Storage. *J. Am. Chem. Soc.* **2022**, *144* (3), 1069-1081.
6. Mayer, J. M., Bonds over Electrons: Proton Coupled Electron Transfer at Solid–Solution Interfaces. *J. Am. Chem. Soc.* **2023**, *145* (13), 7050-7064.
7. Conway, B. E.; Tilak, B. V., Chemical Identity of Adsorbed Intermediates in Electrocatalysis. In *Advances in Catalysis*, Eley, D. D.; Pines, H.; Weisz, P. B., Eds. Academic Press: New York, NY, 1992; Vol. 38, pp 16-18.
8. Falling, L. J.; Velasco-Vélez, J. J.; Mom, R. V.; Knop-Gericke, A.; Schlögl, R.; Teschner, D.; Jones, T. E., The ladder towards understanding the oxygen evolution reaction. *Curr. Opin. Electrochem.* **2021**, *30*, 100842.
9. Cody, C. C.; Brudvig, G. W., Forging O–O Bonds. *Joule* **2021**, *5* (8), 1923-1925.
10. Zhang, M.; de Respinis, M.; Frei, H., Time-resolved observations of water oxidation intermediates on a cobalt oxide nanoparticle catalyst. *Nat. Chem.* **2014**, *6* (4), 362-367.
11. Warburton, R. E.; Mayer, J. M.; Hammes-Schiffer, S., Proton-Coupled Defects Impact O–H Bond Dissociation Free Energies on Metal Oxide Surfaces. *J. Phys. Chem. Lett.* **2021**, *12* (40), 9761-9767.
12. Esch, F.; Fabris, S.; Zhou, L.; Montini, T.; Africh, C.; Fornasiero, P.; Comelli, G.; Rosei, R., Electron Localization Determines Defect Formation on Ceria Substrates. *Science* **2005**, *309* (5735), 752-755.
13. Proe, K. R.; Schreiber, E.; Matson, E. M., Proton-Coupled Electron Transfer at the Surface of Polyoxovanadate-Alkoxide Clusters. *Acc. Chem. Res.* **2023**, *56* (12), 1602-1612.
14. Agarwal, R. G.; Kim, H.-J.; Mayer, J. M., Nanoparticle O–H Bond Dissociation Free Energies from Equilibrium Measurements of Cerium Oxide Colloids. *J. Am. Chem. Soc.* **2021**, *143* (7), 2896-2907.
15. Samantaray, Y.; Martin, D. J.; Agarwal, R. G.; Gibson, N. J.; Mayer, J. M., Proton-Coupled Electron Transfer of Cerium Oxide Nanoparticle Thin-Film Electrodes. *J. Phys. Chem. C* **2023**, *127* (8), 4015-4020.
16. Bernal, S.; Calvino, J. J.; Cifredo, G. A.; Gatica, J. M.; Omil, J. A. P.; Pintado, J. M., Hydrogen chemisorption on ceria: influence of the oxide surface area and degree of reduction. *J. Chem. Soc., Faraday Trans.* **1993**, *89* (18), 3499-3505.
17. Werner, K.; Weng, X.; Calaza, F.; Sterrer, M.; Kropp, T.; Paier, J.; Sauer, J.; Wilde, M.; Fukutani, K.; Shaikhutdinov, S.; Freund, H.-J., Toward an Understanding of Selective Alkyne Hydrogenation on Ceria: On the Impact of O Vacancies on H₂ Interaction with CeO₂(111). *J. Am. Chem. Soc.* **2017**, *139* (48), 17608-17616.
18. Agarwal, R. G.; Coste, S. C.; Groff, B. D.; Heuer, A. M.; Noh, H.; Parada, G. A.; Wise, C. F.; Nichols, E. M.; Warren, J. J.; Mayer, J. M., Free Energies of Proton-Coupled Electron Transfer Reagents and Their Applications. *Chem. Rev.* **2021**, *122* (1), 1-49.
19. Noh, H.; Mayer, J. M., Medium-Independent Hydrogen Atom Binding Isotherms of Nickel Oxide Electrodes. *Chem* **2022**, *8* (12), 3324-3345.

20. Ding, H.; Liu, H.; Chu, W.; Wu, C.; Xie, Y., Structural Transformation of Heterogeneous Materials for Electrocatalytic Oxygen Evolution Reaction. *Chem. Rev.* **2021**, *121* (21), 13174-13212.
21. Nørskov, J. K.; Bligaard, T.; Logadottir, A.; Kitchin, J. R.; Chen, J. G.; Pandelov, S.; Stimming, U., Trends in the Exchange Current for Hydrogen Evolution. *J. Electrochem. Soc.* **2005**, *152* (3), J23-J26.
22. Ooka, H.; Nakamura, R., Shift of the Optimum Binding Energy at Higher Rates of Catalysis. *J. Phys. Chem. Lett.* **2019**, *10* (21), 6706-6713.
23. Wise, C. F.; Mayer, J. M., Electrochemically Determined O–H Bond Dissociation Free Energies of NiO Electrodes Predict Proton-Coupled Electron Transfer Reactivity. *J. Am. Chem. Soc.* **2019**, *141* (38), 14971-14975.
24. Schreiber, E.; Fertig, A. A.; Brennessel, W. W.; Matson, E. M., Oxygen-Atom Defect Formation in Polyoxovanadate Clusters via Proton-Coupled Electron Transfer. *J. Am. Chem. Soc.* **2022**, *144* (11), 5029-5041.
25. Quaino, P.; Juarez, F.; Santos, E.; Schmickler, W., Volcano plots in hydrogen electrocatalysis – uses and abuses. *Beilstein J. Nanotechnol.* **2014**, *5*, 846-854.
26. Medford, A. J.; Vojvodic, A.; Hummelshøj, J. S.; Voss, J.; Abild-Pedersen, F.; Studt, F.; Bligaard, T.; Nilsson, A.; Nørskov, J. K., From the Sabatier principle to a predictive theory of transition-metal heterogeneous catalysis. *J. Catal.* **2015**, *328*, 36-42.
27. Peper, J. L.; Gentry, N. E.; Boudy, B.; Mayer, J. M., Aqueous TiO₂ Nanoparticles React by Proton-Coupled Electron Transfer. *Inorg. Chem.* **2021**, *61* (2), 767-777.
28. Finklea, H. O., Titanium Dioxide (TiO₂) and Strontium Titanate (SrTiO₃). In *Semiconductor Electrodes*, Finklea, H. O., Ed. Elsevier: Amsterdam, 1988; pp 42-154.
29. Makivić, N.; Cho, J.-Y.; Harris, K. D.; Tarascon, J.-M.; Limoges, B.; Balland, V., Evidence of Bulk Proton Insertion in Nanostructured Anatase and Amorphous TiO₂ Electrodes. *Chem. Mater.* **2021**, *33* (9), 3436-3448.
30. Reier, T.; Teschner, D.; Lunkenbein, T.; Bergmann, A.; Selve, S.; Kraehnert, R.; Schlögl, R.; Strasser, P., Electrocatalytic Oxygen Evolution on Iridium Oxide: Uncovering Catalyst-Substrate Interactions and Active Iridium Oxide Species. *J. Electrochem. Soc.* **2014**, *161* (9), F876.
31. Kluge, R. M.; Haid, R. W.; Bandarenka, A. S., Assessment of active areas for the oxygen evolution reaction on an amorphous iridium oxide surface. *J. Catal.* **2021**, *396*, 14-22.
32. Deka, N.; Jones, T. E.; Falling, L. J.; Sandoval-Diaz, L.-E.; Lunkenbein, T.; Velasco-Velez, J.-J.; Chan, T.-S.; Chuang, C.-H.; Knop-Gericke, A.; Mom, R. V., On the Operando Structure of Ruthenium Oxides during the Oxygen Evolution Reaction in Acidic Media. *ACS Catal.* **2023**, *13* (11), 7488-7498.
33. Zhang, L.; Jang, H.; Liu, H.; Kim, M. G.; Yang, D.; Liu, S.; Liu, X.; Cho, J., Sodium-Decorated Amorphous/Crystalline RuO₂ with Rich Oxygen Vacancies: A Robust pH-Universal Oxygen Evolution Electrocatalyst. *Angew. Chem. Int. Ed.* **2021**, *60* (34), 18821-18829.
34. Liu, J.; Goetjen, T. A.; Wang, Q.; Knapp, J. G.; Wasson, M. C.; Yang, Y.; Syed, Z. H.; Delferro, M.; Notestein, J. M.; Farha, O. K.; Hupp, J. T., MOF-enabled confinement and related effects for chemical catalyst presentation and utilization. *Chem. Soc. Rev.* **2022**, *51* (3), 1045-1097.
35. Zhang, X.; Tong, S.; Huang, D.; Liu, Z.; Shao, B.; Liang, Q.; Wu, T.; Pan, Y.; Huang, J.; Liu, Y.; Cheng, M.; Chen, M., Recent advances of Zr based metal organic frameworks

- photocatalysis: Energy production and environmental remediation. *Coord. Chem. Rev.* **2021**, *448*, 214177.
36. Bavykina, A.; Kolobov, N.; Khan, I. S.; Bau, J. A.; Ramirez, A.; Gascon, J., Metal–Organic Frameworks in Heterogeneous Catalysis: Recent Progress, New Trends, and Future Perspectives. *Chem. Rev.* **2020**, *120* (16), 8468-8535.
37. Ahmed, I.; Mondol, M. M. H.; Jung, M. J.; Lee, G. H.; Jhung, S. H., MOFs with bridging or terminal hydroxo ligands: Applications in adsorption, catalysis, and functionalization. *Coord. Chem. Rev.* **2023**, *475*, 214912.
38. Abazari, R.; Sanati, S.; Bajaber, M. A.; Javed, M. S.; Junk, P. C.; Nanjundan, A. K.; Qian, J.; Dubal, D. P., Design and Advanced Manufacturing of NU-1000 Metal–Organic Frameworks with Future Perspectives for Environmental and Renewable Energy Applications. *Small*, 2306353.
39. Fernández-Conde, C.; Romero-Ángel, M.; Rubio-Gaspar, A.; Martí-Gastaldo, C., Engineering of Metal Active Sites in MOFs. In *Catalysis in Confined Frameworks*, 2024; pp 1-66.
40. Kinik, F. P.; Ortega-Guerrero, A.; Ongari, D.; Ireland, C. P.; Smit, B., Pyrene-based metal organic frameworks: from synthesis to applications. *Chem. Soc. Rev.* **2021**, *50* (5), 3143-3177.
41. Noh, H.; Cui, Y.; Peters, A. W.; Pahls, D. R.; Ortuño, M. A.; Vermeulen, N. A.; Cramer, C. J.; Gagliardi, L.; Hupp, J. T.; Farha, O. K., An Exceptionally Stable Metal–Organic Framework Supported Molybdenum(VI) Oxide Catalyst for Cyclohexene Epoxidation. *J. Am. Chem. Soc.* **2016**, *138* (44), 14720-14726.
42. Noh, H.; Kung, C.-W.; Otake, K.-i.; Peters, A. W.; Li, Z.; Liao, Y.; Gong, X.; Farha, O. K.; Hupp, J. T., Redox-Mediator-Assisted Electrocatalytic Hydrogen Evolution from Water by a Molybdenum Sulfide-Functionalized Metal–Organic Framework. *ACS Catal.* **2018**, *8* (10), 9848-9858.
43. Noh, H.; Yang, Y.; Ahn, S.; Peters, A. W.; Farha, O. K.; Hupp, J. T., Molybdenum Sulfide within a Metal–Organic Framework for Photocatalytic Hydrogen Evolution from Water. *J. Electrochem. Soc.* **2019**, *166* (5), H3154-H3158.
44. Noh, H.; Yang, Y.; Zhang, X.; Goetjen, T. A.; Syed, Z. H.; Lu, Z.; Ahn, S.; Farha, O. K.; Hupp, J. T., Single-Site, Single-Metal-Atom, Heterogeneous Electrocatalyst: Metal–Organic-Framework Supported Molybdenum Sulfide for Redox Mediator-Assisted Hydrogen Evolution Reaction. *ChemElectroChem* **2020**, *7* (2), 509-516.
45. Lammert, M.; Glißmann, C.; Reinsch, H.; Stock, N., Synthesis and Characterization of New Ce(IV)-MOFs Exhibiting Various Framework Topologies. *Cryst. Growth Des.* **2017**, *17* (3), 1125-1131.
46. Smolders, S.; Lomachenko, K. A.; Bueken, B.; Struyf, A.; Bugaev, A. L.; Atzori, C.; Stock, N.; Lamberti, C.; Roeffaers, M. B. J.; De Vos, D. E., Unravelling the Redox-catalytic Behavior of Ce⁴⁺ Metal–Organic Frameworks by X-ray Absorption Spectroscopy. *ChemPhysChem* **2018**, *19* (4), 373-378.
47. Wu, X.-P.; Gagliardi, L.; Truhlar, D. G., Cerium Metal–Organic Framework for Photocatalysis. *J. Am. Chem. Soc.* **2018**, *140* (25), 7904-7912.
48. Jacobsen, J.; Ienco, A.; D'Amato, R.; Costantino, F.; Stock, N., The chemistry of Ce-based metal–organic frameworks. *Dalton Trans.* **2020**, *49* (46), 16551-16586.
49. Shen, C.-H.; Chuang, C.-H.; Gu, Y.-J.; Ho, W. H.; Song, Y.-D.; Chen, Y.-C.; Wang, Y.-C.; Kung, C.-W., Cerium-Based Metal–Organic Framework Nanocrystals Interconnected by

Carbon Nanotubes for Boosting Electrochemical Capacitor Performance. *ACS Appl. Mater. Interfaces* **2021**, *13* (14), 16418-16426.

50. Chlistunoff, J.; Sansiñena, J.-M., On the use of Nafion® in electrochemical studies of carbon supported oxygen reduction catalysts in aqueous media. *J. Electroanal. Chem.* **2016**, *780*, 134-146.

51. Jackson, M. N.; Pegis, M. L.; Surendranath, Y., Graphite-Conjugated Acids Reveal a Molecular Framework for Proton-Coupled Electron Transfer at Electrode Surfaces. *ACS Cent. Sci.* **2019**, *5* (5), 831-841.

52. Amombo Noa, F. M.; Abrahamsson, M.; Ahlberg, E.; Cheung, O.; Göb, C. R.; McKenzie, C. J.; Öhrström, L., A unified topology approach to dot-, rod-, and sheet-MOFs. *Chem* **2021**, *7* (9), 2491-2512.

53. Lyon, L. A.; Hupp, J. T., Energetics of the Nanocrystalline Titanium Dioxide/Aqueous Solution Interface: Approximate Conduction Band Edge Variations between $H_0 = -10$ and $H = +26$. *J. Phys. Chem. B* **1999**, *103* (22), 4623-4628.

54. Wise, C. F.; Agarwal, R. G.; Mayer, J. M., Determining Proton-Coupled Standard Potentials and X-H Bond Dissociation Free Energies in Nonaqueous Solvents Using Open-Circuit Potential Measurements. *J. Am. Chem. Soc.* **2020**, *142* (24), 10681-10691.

55. Wang, J.; Gan, L.; Zhang, W.; Peng, Y.; Yu, H.; Yan, Q.; Xia, X.; Wang, X., In situ formation of molecular Ni-Fe active sites on heteroatom-doped graphene as a heterogeneous electrocatalyst toward oxygen evolution. *Sci. Adv.* **2018**, *4* (3), eaap7970.

56. Nakagawa, T.; Beasley, C. A.; Murray, R. W., Efficient Electro-Oxidation of Water near Its Reversible Potential by a Mesoporous IrO_x Nanoparticle Film. *J. Phys. Chem. C* **2009**, *113* (30), 12958-12961.

57. Slopes between 50 - 70 mV/pH have been interpreted as 'close-to-59 mV/pH' in previous literature. See refs. 15, 19, 50, 51, and 58 for details.

58. Nedzbala, H. S.; Westbroek, D.; Margavio, H. R. M.; Yang, H.; Noh, H.; Magpantay, S. V.; Donley, C. L.; Kumbhar, A. S.; Parsons, G. N.; Mayer, J. M., Photoelectrochemical Proton-Coupled Electron Transfer of TiO₂ Thin Films on Silicon. *J. Am. Chem. Soc.* **2024**, DOI: jacs.4c00014.

59. Maheswari, N.; Muralidharan, G., Hexagonal CeO₂ nanostructures: an efficient electrode material for supercapacitors. *Dalton Trans.* **2016**, *45* (36), 14352-14362.

60. Bard, A. J.; Faulkner, L. R., Double-Layer Structure and Adsorption. In *Electrochemical Methods: Fundamentals and Applications*, John Wiley & Sons Inc.: New York, NY, 2001; pp 534-579.

61. Surendranath, Y.; Dincă, M.; Nocera, D. G., Electrolyte-Dependent Electrosynthesis and Activity of Cobalt-Based Water Oxidation Catalysts. *J. Am. Chem. Soc.* **2009**, *131* (7), 2615-2620.

62. Dincă, M.; Surendranath, Y.; Nocera, D. G., Nickel-borate oxygen-evolving catalyst that functions under benign conditions. *Proc. Nat. Acad. Sci.* **2010**, *107* (23), 10337-10341.

63. Ardizzone, S.; Fregonara, G.; Trasatti, S., "Inner" and "outer" active surface of RuO₂ electrodes. *Electrochim. Acta* **1990**, *35* (1), 263-267.

64. Levi, M. D.; Aurbach, D., Frumkin intercalation isotherm — a tool for the description of lithium insertion into host materials: a review. *Electrochim. Acta* **1999**, *45* (1), 167-185.

65. Bard, A. J.; Faulkner, L. R., Electroactive Layers and Modified Electrodes. In *Electrochemical Methods: Fundamentals and Applications*, John Wiley & Sons Inc.: New York, NY, 2001; pp 580-631.

66. Pourbaix, M., *Atlas of Electrochemical Equilibria in Aqueous Solution*. Houston, TX, 1974.
67. Hayes, S. A.; Yu, P.; O'Keefe, T. J.; O'Keefe, M. J.; Stoffer, J. O., The Phase Stability of Cerium Species in Aqueous Systems : I. E-pH Diagram for the System. *J. Electrochem. Soc.* **2002**, *149* (12), C623.
68. Adamo, C.; Barone, V., Toward reliable density functional methods without adjustable parameters: The PBE0 model. *J. Chem. Phys.* **1999**, *110* (13), 6158-6170.
69. Hutter, J.; Iannuzzi, M.; Schiffmann, F.; VandeVondele, J., CP2K: Atomistic simulations of condensed matter systems. *Wiley Interdiscip. Rev.: Comput. Mol. Sci.* **2014**, *4* (1), 15-25.
70. Momeni, M. R.; Cramer, C. J., Computational Screening of Roles of Defects and Metal Substitution on Reactivity of Different Single- vs Double-Node Metal–Organic Frameworks for Sarin Decomposition. *J. Phys. Chem. C* **2019**, *123* (24), 15157-15165.
71. Hariharan, P. C.; Pople, J. A., The influence of polarization functions on molecular orbital hydrogenation energies. *Theoret. Chim. Acta* **1973**, *28* (3), 213-222.
72. Dolg, M.; Stoll, H.; Preuss, H., Energy-adjusted ab initio pseudopotentials for the rare earth elements. *J. Chem. Phys.* **1989**, *90* (3), 1730-1734.
73. Rabuck, A. D.; Scuseria, G. E., Improving self-consistent field convergence by varying occupation numbers. *J. Chem. Phys.* **1999**, *110* (2), 695-700.
74. Liu, B.; Baumann, A. E.; Butala, M. M.; Thoi, V. S., Phosphate-functionalized Zirconium Metal–Organic Frameworks for Enhancing Lithium–Sulfur Battery Cycling. *Chem. Eur. J.* **2023**, *29* (40), e202300821.
75. Hod, I.; Bury, W.; Gardner, D. M.; Deria, P.; Roznyatovskiy, V.; Wasielewski, M. R.; Farha, O. K.; Hupp, J. T., Bias-Switchable Permselectivity and Redox Catalytic Activity of a Ferrocene-Functionalized, Thin-Film Metal–Organic Framework Compound. *The Journal of Physical Chemistry Letters* **2015**, *6* (4), 586-591.
76. Palmer, R. H.; Liu, J.; Kung, C.-W.; Hod, I.; Farha, O. K.; Hupp, J. T., Electroactive Ferrocene at or near the Surface of Metal–Organic Framework UiO-66. *Langmuir* **2018**, *34* (16), 4707-4714.
77. Wang, R.; Bukowski, B. C.; Duan, J.; Sui, J.; Snurr, R. Q.; Hupp, J. T., Art of Architecture: Efficient Transport through Solvent-Filled Metal–Organic Frameworks Regulated by Topology. *Chem. Mater.* **2021**, *33* (17), 6832-6840.
78. Bermúdez-García, J. M.; Vicent-Luna, J. M.; Yáñez-Vilar, S.; Hamad, S.; Sánchez-Andújar, M.; Castro-García, S.; Calero, S.; Señarís-Rodríguez, M. A., Liquid self-diffusion of H₂O and DMF molecules in Co-MOF-74: molecular dynamics simulations and dielectric spectroscopy studies. *Phys. Chem. Chem. Phys.* **2016**, *18* (29), 19605-19612.
79. Costentin, C.; Nocera, D. G., Self-healing catalysis in water. *Proc. Nat. Acad. Sci.* **2017**, *114* (51), 13380-13384.
80. Fortunato, J.; Shin, Y. K.; Spencer, M. A.; van Duin, A. C. T.; Augustyn, V., Choice of Electrolyte Impacts the Selectivity of Proton-Coupled Electrochemical Reactions on Hydrogen Titanate. *J. Phys. Chem. C* **2023**, *127* (25), 11810-11821.
81. Burke, M. S.; Zou, S.; Enman, L. J.; Kellon, J. E.; Gabor, C. A.; Pledger, E.; Boettcher, S. W., Revised Oxygen Evolution Reaction Activity Trends for First-Row Transition-Metal (Oxy)hydroxides in Alkaline Media. *J. Phys. Chem. Lett.* **2015**, *6* (18), 3737-3742.
82. Wang, Y.; Yan, D.; El Hankari, S.; Zou, Y.; Wang, S., Recent Progress on Layered Double Hydroxides and Their Derivatives for Electrocatalytic Water Splitting. *Adv. Sci.* **2018**, *5* (8), 1800064.

83. Xie, L. S.; Skorupskii, G.; Dincă, M., Electrically Conductive Metal–Organic Frameworks. *Chem. Rev.* **2020**, *120* (16), 8536-8580.
84. McCarver, G. A.; Hinde, R. J.; Vogiatzis, K. D., Selecting Quantum-Chemical Methods for Lanthanide-Containing Molecules: A Balance between Accuracy and Efficiency. *Inorg. Chem.* **2020**, *59* (15), 10492-10500.
85. Grimmel, S.; Schoendorff, G.; Wilson, A. K., Gauging the Performance of Density Functionals for Lanthanide-Containing Molecules. *J. Chem. Theory Comput.* **2016**, *12* (3), 1259-1266.
86. Gileadi, E., Adsorption in Electrochemistry. In *Electrosorption*, Gileadi, E., Ed. Springer: Boston, MA, 1967; Vol. 1, pp 1-18.
87. Strmcnik, D.; Tripkovic, D.; van der Vliet, D.; Stamenkovic, V.; Marković, N. M., Adsorption of hydrogen on Pt(111) and Pt(100) surfaces and its role in the HOR. *Electrochem. Commun.* **2008**, *10* (10), 1602-1605.
88. Whittaker, E. J. W.; Muntus, R., Ionic radii for use in geochemistry. *Geochim. Cosmochim. Acta* **1970**, *34* (9), 945-956.
89. Mitchell, K. J.; Abboud, K. A.; Christou, G., Atomically-precise colloidal nanoparticles of cerium dioxide. *Nat. Commun.* **2017**, *8* (1), 1445.
90. Lammert, M.; Glißmann, C.; Stock, N., Tuning the stability of bimetallic Ce(IV)/Zr(IV)-based MOFs with UiO-66 and MOF-808 structures. *Dalton Trans.* **2017**, *46* (8), 2425-2429.
91. Wei, Y.-S.; Zhang, M.; Zou, R.; Xu, Q., Metal–Organic Framework-Based Catalysts with Single Metal Sites. *Chem. Rev.* **2020**, *120* (21), 12089-12174.
92. Saouma, C. T.; Richard, S.; Smolders, S.; Delley, M. F.; Ameloot, R.; Vermoortele, F.; De Vos, D. E.; Mayer, J. M., Bulk-to-Surface Proton-Coupled Electron Transfer Reactivity of the Metal–Organic Framework MIL-125. *J. Am. Chem. Soc.* **2018**, *140* (47), 16184-16189.
93. Howarth, A. J.; Liu, Y.; Li, P.; Li, Z.; Wang, T. C.; Hupp, J. T.; Farha, O. K., Chemical, thermal and mechanical stabilities of metal–organic frameworks. *Nat. Rev. Mater.* **2016**, *1* (3), 15018.
94. Klet, R. C.; Liu, Y.; Wang, T. C.; Hupp, J. T.; Farha, O. K., Evaluation of Brønsted acidity and proton topology in Zr- and Hf-based metal–organic frameworks using potentiometric acid–base titration. *J. Mater. Chem. A* **2016**, *4* (4), 1479-1485.
95. Ho, W. H.; Li, S.-C.; Wang, Y.-C.; Chang, T.-E.; Chiang, Y.-T.; Li, Y.-P.; Kung, C.-W., Proton-Conductive Cerium-Based Metal–Organic Frameworks. *ACS Appl. Mater. Interfaces* **2021**, *13* (46), 55358-55366.
96. Trummal, A.; Lipping, L.; Kaljurand, I.; Koppel, I. A.; Leito, I., Acidity of Strong Acids in Water and Dimethyl Sulfoxide. *J. Phys. Chem. A* **2016**, *120* (20), 3663-3669.
97. Luo, Y.-R., *Comprehensive Handbook of Chemical Bond Energies*. CRC Press: Boca Raton, FL, 2007.
98. Wise, C. F.; Mayer, J. M., Correction to “Electrochemically Determined O–H Bond Dissociation Free Energies of NiO Electrodes Predict Proton-Coupled Electron Transfer Reactivity”. *J. Am. Chem. Soc.* **2020**, *142* (28), 12544-12545.
99. Wang, F.; Stahl, S. S., Electrochemical Oxidation of Organic Molecules at Lower Overpotential: Accessing Broader Functional Group Compatibility with Electron–Proton Transfer Mediators. *Acc. Chem. Res.* **2020**, *53* (3), 561-574.
100. Chiang, Y.-T.; Gu, Y.-J.; Song, Y.-D.; Wang, Y.-C.; Kung, C.-W., Cerium-based metal–organic framework as an electrocatalyst for the reductive detection of dopamine. *Electrochem. Commun.* **2022**, *135*, 107206.

101. Jodko-Piórecka, K.; Sikora, B.; Kluzek, M.; Przybylski, P.; Litwinienko, G., Antiradical Activity of Dopamine, L-DOPA, Adrenaline, and Noradrenaline in Water/Methanol and in Liposomal Systems. *J. Org. Chem.* **2022**, *87* (3), 1791-1804.

